J Mater Sci (2009) 44:1127–1136
DOI 10.1007/s10853-008-3194-9

Failure behavior of Cu–Ti–Zr-based bulk metallic glass alloys

Medhat Awad El-Hadek · Magdy Kassem

Received: 22 October 2008 / Accepted: 12 December 2008 / Published online: 22 January 2009

Abstract Microstructure fracture and mechanical properties of Cu-based bulk metallic glass alloys were investigated. Centrifugal casting into copper molds were used to manufacture basic $Cu_{47}Ti_{33}Zr_{11}Ni_9$, and modified $Cu_{47}Ti_{33}Zr_{11}Ni_7Si_1Sn_1$ alloys. Although the alloys show an amorphous structure, TEM images revealed the formation of nanoparticles. At room temperature compression tests reveal fracture strength of 2000 MPa, elastic modulus of 127 GPa, and 1.8% fracture strain for the unmodified basic alloy. Whereas the modified alloy exhibits a fracture strength of 2179 MPa, elastic modulus reaches 123 GPa, and 2.4% fracture strain. So, with the addition of 1 at.% Si and Sn, the fracture strength improves by 9% and the fracture strain improves by 25%, but the fracture behavior under compression conditions exhibits a conical shape similar to that produced by tensile testing of ductile alloys. A proposed fracture mechanism explaining the formation of the conical fracture surface was adopted. The formation of homogeneously distributed nano-size (2–5 nm) precipitates changes the mode of fracture of the metallic glass from single to multiple shear plane modes leading to the conical shape fracture surface morphology.

M. A. El-Hadek (✉)
Department of Mechanical Design & Production, Faculty of Engineering, Suez Canal University, Port-Said, Egypt
e-mail: m.elhadek@scuegypt.edu.eg; melhadex@gmail.com

M. Kassem
Department of Metallurgy, Faculty of Petroleum & Mining Engineering, Suez Canal University, Suez, Egypt
e-mail: mkassem54@yahoo.com

Introduction

Recently, the development of multi-component metallic glasses with good glass-forming ability and high thermal stability has made it possible to obtain bulk glass specimens at moderate cooling rates achievable by conventional solidification techniques [1, 2]. These bulk metallic glasses (BMG) have such promising properties as high yield strength, hardness, and elastic strain limit, along with relatively high fracture toughness, fatigue resistance, and corrosion resistance [3–5]. Copper-based bulk metallic glasses are reported to exhibit high strength and low price. Therefore, the most recent researchers have been driven to identify highly processable Cu-based alloys with high glass-forming ability [5, 6].

The modified Cu–Ti–Zr–Ni–Si–Sn alloys investigated in this study are reported to show a high glass-forming ability and a large super-cooled liquid region before crystallization [7]. Glade et al. [8] reported that upon heating copper-enriched and titanium-enriched regions primarily decompose in the amorphous matrix prior to crystallization. The nanocrystals are identified as a face-centered cubic phase with a lattice parameter of $a = 0.36$ nm [9]. Moreover, it has been reported that small additions of Si, Pb, Ag, and Sn enhance the stability and glass-forming ability of selected bulk metallic glass alloys [10]. In the Cu–Ti–Zr–Ni–Si–Sn system, by increasing the Sn content up to 2 atomic percentages the maximum diameter of the BMG increases to 6 mm, followed by a decrease [11]. Alloys with more than 6 at.% of Sn show low glass-forming ability.

For silicon, small additions between 0.5 and 1 at.% increase the attainable maximum thickness of glass ingots from 4 to 7 mm [12]. Thermal analysis reveals that neither the thermodynamics nor the kinetics of the alloys were significantly affected by the Si addition. This led to the suggestion that Si enhances the glass-forming ability by chemically passivating impurities such as oxygen that cause heterogeneous nucleation in the melt [12, 13]. For Ni-Pd-P alloys, it was shown by Volkert [14] that the addition of 1 at.% Si improves the thermal stability of the super-cooled liquid of this system of alloys. In this case, the improvement by adding Si was attributed to the destabilization of P_2O_5 clusters that were considered to act as heterogeneous nucleation sites. Also, Choi-Yim et al. [12] suggested that for the $Cu_{47}Ti_{33}Zr_{11}Ni_9$ alloy, Si might act in a similar way, i.e., Si might help to destabilize TiO_2 clusters present in the melt.

Furthermore, it has been reported that Pb, Si, and B additions in the ppm range are very effective in alleviating the harmful effect of oxygen impurities in Zr-based BMGs, and enhance the thermal stability [10]. The beneficial effect of micro-alloying was attributed to the reaction of these elements with oxygen and the formation of innocuous second-phase particles.

Bulk metallic glasses demonstrate significant mechanical properties, such as high strength and large elastic strain at room temperature, but they typically fail after limited macroscopic plastic strain. The limited plastic strain is attributed to the inhomogeneous deformation behavior. This inhomogeneous deformation behavior is correlated to the formation of highly localized shear bands and the overall strain, which is determined by the number of shear bands [12, 15]. Although the local plastic strain in a shear band is quite large, only a few shear bands are active, which leads to catastrophic failure under unconstrained conditions without macroscopic plasticity at room temperature [10, 11, 16, 17].

Recently, the mechanical properties of the glass-reinforced composites were modeled by using the iso-stress Reuss model that allows the prediction of the mechanical properties of a composite from the volume-weighted averages of the components properties [18]. The Gd–Ni–Al bulk glassy alloys with great glass-forming ability and good mechanical properties are reported to be formed obtained by common copper mold casting [19]. Under compressive loading conditions, metallic glasses deform and fracture occurs along the localized shear planes. The fracture angle, θ_C, between the compressive axis and the shear plane is generally smaller than 45° (about 42°) [19]. Deviation from the maximum shear stress plane (45°) indicates that the fracture behavior of the metallic glass under compressive and tensile load does not follow the von Mises criterion [20–23]. Donovan [24] has proposed a yield criterion for $Pd_{40}Ni_{40}P_{20}$ metallic glass under compressive load. He found that the yield behavior of the glass follows a Mohr–Coulomb criterion rather than the Von Mises criterion, since the difference in the fracture angles θ_C and θ_T is quite large, and the angle of the shear plane is, in general, smaller than 45°.

Bhowmick [25] reported the promotion of crystallization with the increase of oxygen concentration. Zhang et al. [26] argued that, since metallic glass acts globally as a homogeneous material, therefore the critical shear fracture stress acts on any plane under the condition without normal stress. However, since the fracture angles in case of compressive and tensile loading (θ_C and θ_T) always deviate from 45°, the normal stress must play an important role in the fracture processes of metallic glasses. Donovan [24] and Liu et al. [27] also attributed the deviation of the fracture angle from 45° to the effect of normal stress. Other methods for producing fiber BMG were also reported [28]. Under symmetrically cyclic stress control, the life of tungsten fiber-reinforced amorphous alloy was much longer than that of the monolithic amorphous alloy [28].

In the quest for modifying the newly developed Cu-base BMGs, one way is to introduce some precipitates in order to change the deformation mode for enhancing the toughness and mechanical properties of such alloys. The subject of this paper is to study the effect of alloying $Cu_{47}Ti_{33}Zr_{11}Ni_9$ glass with Si and Sn and to investigate the influence of these alloying additions on the room temperature compression properties and the fracture mode.

Experimental

$Cu_{47}Ti_{33}Zr_{11}Ni_{9-(x+y)}$ (x = Si, y = Sn, $0 \le x \le 1$, $0 \le y \le 2$) master alloys were prepared by arc-melting pure metals with purities of 99.99 wt% in a Ti-gettered argon atmosphere (99.9999% purity). From these master alloys, cylindrical bulk samples with 3 mm diameter and 80 mm length were prepared by centrifugal casting into a copper mold in an argon atmosphere of 99.99% purity. Rapidly solidified ribbons with 6 mm width and about 30 μm thickness were produced by single roller melt spinning technique under argon atmosphere. Structural investigations of specimens taken from the bottom of the rods (higher cooling rate) were done by X-ray diffraction (XRD) using an HZG 4 diffractometer with Cu Kα radiation. Transmission Electron Microscopy (TEM) was also performed with a Jeol 2000FX analytical microscope operated at 200 kV to capture fine formations that SEM imaging are limited at. High Resolution Transmission Electron Microscopy (HRTEM) type FEI Tecnai F30 Super TWIN with a Schottky field emitter, using an acceleration voltage of 300 kV, point resolution limit 0.2 nm was used. The HRTEM is equipped with an STEM (Scanning Transmission Electron Microscope) unit (smallest probe size 0.2 nm) and an EDAX-EDX system using a Si Detector. For TEM, the specimens were grinded, mechanically dimpled, and thinned by Ar ion milling. The thermal stability of the glass samples was analyzed by differential scanning calorimetry using a Perkin-Elmer DSC7 at a heating rate of 20 K min^{-1} under a flowing argon atmosphere. Room temperature compression tests were done with an Instron 8562 electromechanical testing machine under quasi-static loading (strain rate of 8×10^{-5} to 1.3×10^{-4} s^{-1}). From the cast rods, cylindrical specimens with 3 mm diameter and 5.5 mm height were prepared. In order to avoid effects of friction between the specimen and the punches, the contact surfaces of the samples were grinded and polished. The samples were deformed until fracture occurred, and to insure consistency and homogeneity, a minimum of three samples for each case were subjected to the same loading conditions and an average value were taken, and presented in the results, where the measurement variation were less than 8%. Vickers microhardness, H_v, measurements were conducted using a Neophot hardness tester and a load of 0.1–1 N applied for 10 s, and also to insure consistency thoughout the material surface and homogeneity, a minimum of ten readings were taken for each case, and the average was presented in the results, where the measurement variation was less than 6%.

Results and discussion

The X-ray diffraction pattern of $Cu_{47}Ti_{33}Zr_{11}Ni_9$ shows an amorphous structure with no apparent crystalline peaks, as presented in Fig. 1. No apparent difference in the diffraction pattern was observed for the modified $Cu_{47}Ti_{33}Zr_{11}Ni_7Si_1Sn_1$ alloys.

For the rapidly solidified ribbons, the addition of 1 at.% Si and 1 at.% Sn has increased the width of the supercooled liquid region, DT_x, between onset of the glass transition T_g and onset of primary crystallization, T_{x_1}. The DSC scan of the modified $Cu_{47}Ti_{33}Zr_{11}Ni_7Si_1Sn_1$ alloys shows three exothermic peaks, corresponding to the stepwise crystallization of the alloy. The onset glass transition temperature, T_g, is about 732 K and the crystallization onset temperature (T_x) for the three peaks are $T_{x_1} = 776$ K, $T_{x_2} = 819$ K, and $T_{x_3} = 862$ at a heating rate of 40 K min^{-1}, as presented in Fig. 2. Cast 3 mm rods of the same composition show only a slight (2 K) difference from the values of the as-spun ribbons. The previous values were also evaluated for two 3 mm specimens from the rod bottom and the next up. The values for both specimens were also very close.

TEM investigation proved that the as-cast 3 mm diameter rods of the unmodified $Cu_{47}Ti_{33}Zr_{11}Ni_9$ alloy was fully glassy, as reported through the literature [6, 27]. The structural investigation of the modified $Cu_{47}Ti_{33}Zr_{11}Ni_7Si_1Sn_1$ alloys using TEM reveals a structure of an amorphous phase with a sharp diffuse ring pattern, as presented in Fig. 3a, which implies the presence of nanosize crystallites. At higher magnification, as presented in Fig. 3b, the bright-field image and the corresponding diffraction pattern shows very fine (2–5 nm) crystallites. At lower cooling rate (upper part of the specimen), the nanocrystalline precipitates are larger in size (up to 50 nm) and some 0.5 μm large primary dendrites with bcc β-Ti structure form. EDX analysis indicates that the average composition of the dendritic phase is $Ti_{54.7}Ni_{13.7}Cu_{23}Zr_{8.7}$ [22].

The addition of Si and Sn plays an important role in modifying the microstructure. Silicon is suggested to destabilize Ti-oxides [12, 13]. Such oxides form in a small number and can serve as heterogeneous nucleation centers. Silicon-rich dendrites of about 500 nm in size are shown in Fig. 4a.

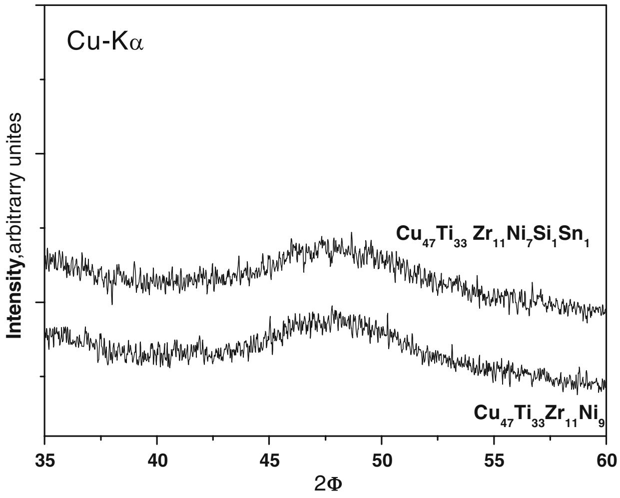

Fig. 1 X-ray diffraction pattern of modified and non modified Cu-base alloy

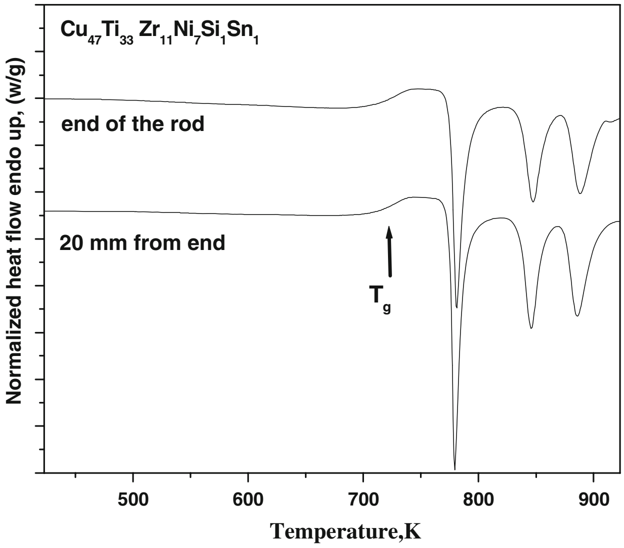

Fig. 2 DSC thermogram for the modified Cu-base BMG

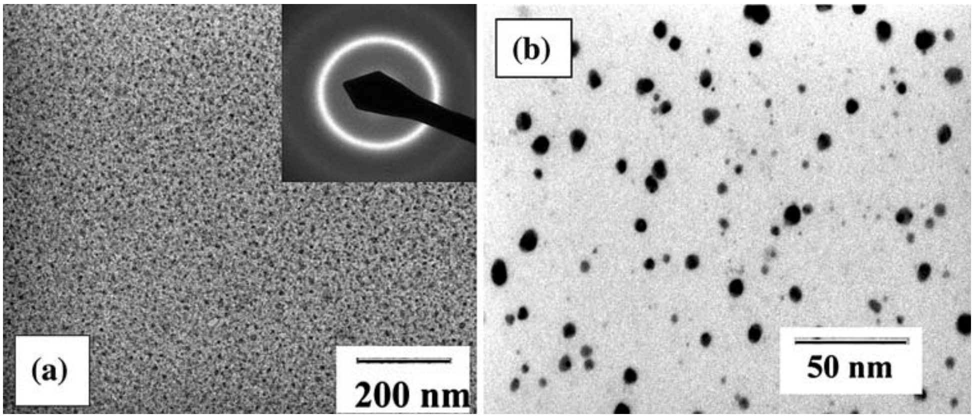

Fig. 3 **a** Bright field and diffraction pattern of modified $Cu_{47}Ti_{33}Zr_{11}Ni_7Si_1Sn_1$ alloy showing a narrow diffuse ring, and **b** higher magnification of A, showing the very fine Copper rich nanoparticles

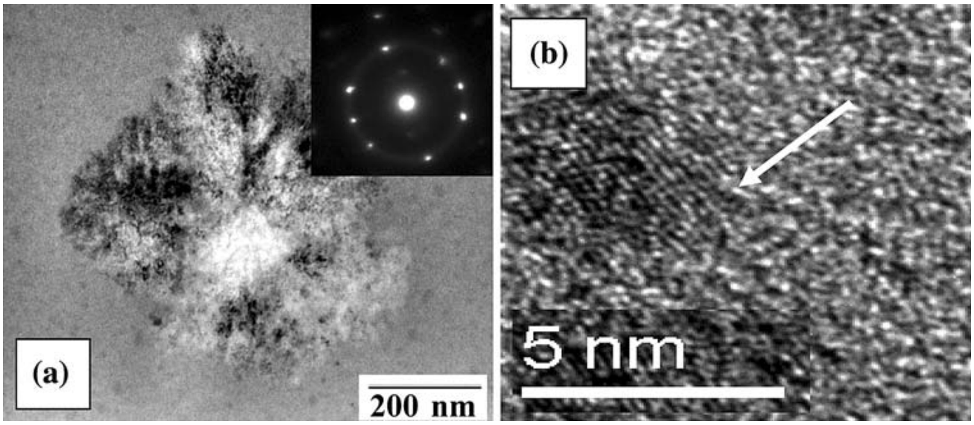

Fig. 4 For the modified alloy **a** bright field image and diffraction pattern of Si-rich dendrites, and **b** HTEM dark field image showing the lattice fringes of the less than 5 nano particles (as pointed out with the white arrow)

EDX analysis of these dendrites reveals a silicon content of 1.2–6.5 at.%. At the same time the majority of the nucleation during crystallization takes place by homogeneous nucleation due to prior removal of oxygen. A range of sizes (5–50 nm) of Cu-rich nanocrystallites is observed. The fine nanoparticles are resolved by HRTEM where lattice fringes of such crystals are evident, as presented in Fig. 4b. These nanoparticles are homogeneously distributed in the glassy matrix. Also, relatively larger particles of about 50 nm are observed in Fig. 3b. A high-angle angular field image (STEM) of the Cu-rich nanocrystallites, as presented in Fig. 5a. The EDX analysis indicates that these particles are Cu-rich as determined from the intensity profile extracted from the EDX spectra for one particle and the surrounding matrix, as shown in Fig. 5b. The EDX spectrum from a Cu-rich particle and the matrix is also presented in Fig. 5c.

The stress–strain curves of the room temperature compression tests carried out for the 3 mm cylinders of the unmodified and the modified alloys, as presented in Fig. 6a, b. The ultimate compression stress for the modified $Cu_{47}Ti_{33}Zr_{11}Ni_7Si_1Sn_1$ alloy reaches about 2180 MPa with 0.67% plastic strain, yielding occurs at 2178 MPa, and fracture strain of 2.4% was recorded, where the Elastic modulus was calculated to be 118 GPa. Whereas for the unmodified basic alloy fracture strength was 2000 MPa, for Elastic modulus it was of 127 GPa, and 1.8% fracture strain.

With the addition of 1 at.% Si and Sn, the fracture strength improves by 9% and the fracture strain improves by 25%. The compression stress–strain behavior for the modified $Cu_{47}Ti_{33}Zr_{11}Ni_7Si_1Sn_1$ alloy but subjected to different cooling rates (four deferent cooling rates, 10, 25, 50, 100 °C s^{-1}) was also tested and presented in Fig. 6b. As the cooling rate decreases Elastic modulus increases and both the ultimate compressive stress and the fracture strain decrease. These changes in the mechanical properties are attributed to the increase in the volume fraction of the nanocrystallites, which in turn controls the deformation behavior of the BMG and leads to embrittling [29]. The mechanical properties of the composite were reported to follow the rule of mixture for the two existing phases (nanocrystals and amorphous) [30].

The Vickers microhardness (H_v), measurements at room temperature for the modified $Cu_{47}Ti_{33}Zr_{11}Ni_7Si_1Sn_1$ alloy were also investigated. No cracks were observed radiating from corners or sides of the Vickers indentation when up to 100 g load was used. This was verified using SEM imaging of the surface through all the tested samples, which indicates high fracture toughness of the material [31]. The

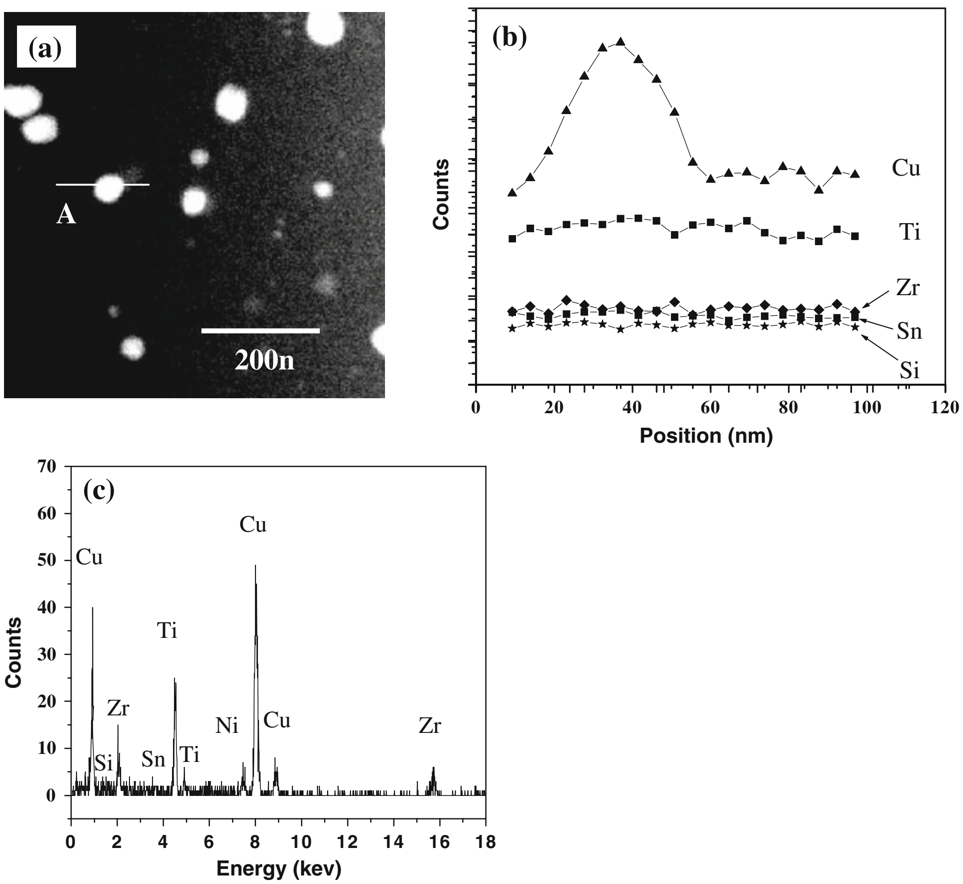

Fig. 5 For the modified alloy **a** High Angle Angular Dark Field image (STEM), **b** Intensity profile extracted from the EDX spectra, and **c** EDX spectrum from a copper-rich particle

hardness value at 5 g load is about 490 and continuously increases up to 660 with increasing load, as presented in Fig. 7.

The increase in hardness may be attributed to the process of continuous crystallization during plastic deformation (indentation). Amorphous alloys have been observed to undergo mechanically induced nanocrystallization. For example, Chen et al. [32] observed the formation of nanocrystalline Al particles within shear bands of amorphous $Al_{90}Fe_5Ce_5$ ribbons bent at room temperature. Formation of nanocrystalline Al was also induced in Al-based amorphous alloys by high-energy ball milling [33]. Al nanocrystal precipitation in amorphous $Al_{90}Fe_5Gd_5$ was also observed within vein protrusions on the tensile fracture surface and along crack propagation paths, as well as within shear bands resulting from bending [34]. The $Cu_{47}Ti_{33}Zr_{11}Ni_9$ alloy shows an apparently inclined fracture surface (about 45° with the applied stress axis) similar to that encountered for a variety of BMGs [27]. The fracture surface exhibits a rough morphology. Close investigation of the surface shows a typical vein structure in the direction of the maximum shear stress, as presented in Fig. 8a, b. The formation of single shear plane is due to the inhomogeneous deformation that leads to localized shear [11].

The examination of the fracture surface of the modified $Cu_{47}Ti_{33}Zr_{11}Ni_7Si_1Sn_1$ alloy shows a peculiar anomaly. A characteristic conical shape failure similar in appearance to that produced by tensile testing of ductile metals was observed for the uniaxially compressed 3 mm diameter cylinders, as presented in Fig. 9.

The conical surface has an angle of about 45° with the compressive stress axis. Close examination of the conical surface reveals a layered morphology with one layer showing a well-defined vein pattern morphology found normally in bulk metallic glass [35] and the other layer with no characteristic features. The vein-like morphology is a typical characteristic of ductile fracture. The layered structure is aligned in the direction of the maximum shear stress. The vein like layer is pulled out relative to the other layer. A large number of traces of inhomogeneous shear bands appear in the outer surface of the cylinder as a sign of increased shear activity, as presented in Fig. 9.

For the modified $Cu_{47}Ti_{33}Zr_{11}Ni_6Si_1Sn_2$ alloy, the surface morphology of the fracture surface becomes irregular with no specific features although some parts of the conical morphology are present, as presented in Fig. 10. Three different local modes of fracture are observed as presented in Fig. 10b–d. In Fig. 10a, the regular vein-shaped morphology shows up, which indicates that the deformation

Fig. 6 Compressive stress strain **a** for two modified and the unmodified Cu-base alloy, **b** for modified alloy at four different cooling rates, 10, 25, 50, 100 °C s^{-1}

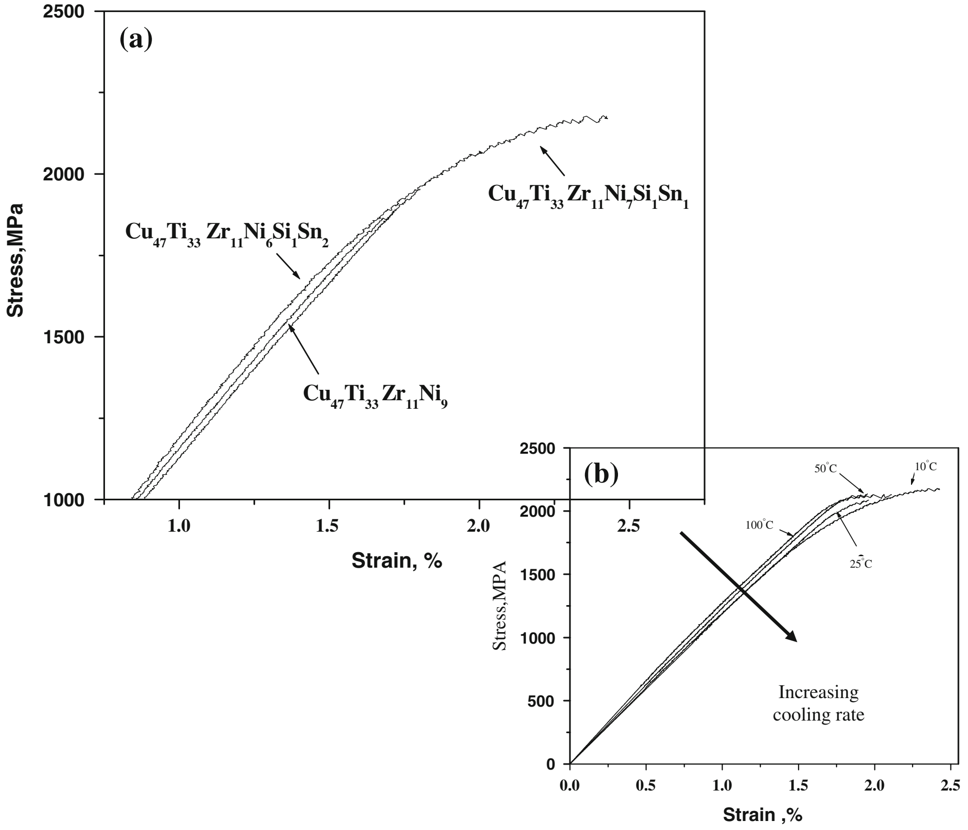

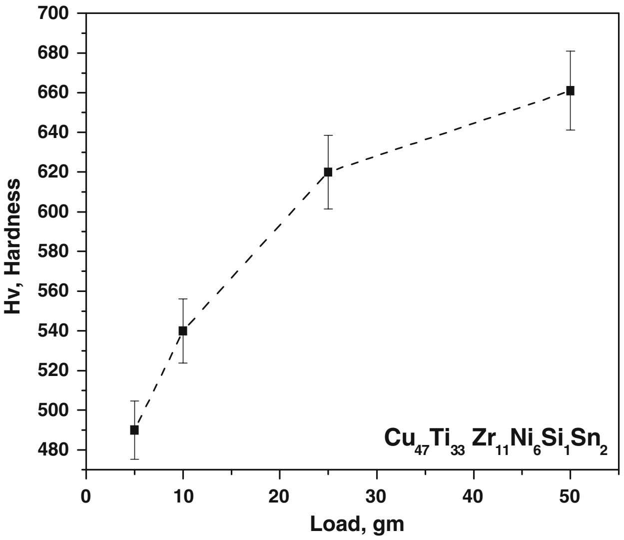

Fig. 7 Hardness measurements at 5 g for the modified Cu-based alloy

due to pure shear. In some regions a mixed mode of fracture occurs (Fig. 10b) and a rough surface with vein-like regions was visible (Fig. 10c). Figure 10d shows the smooth fracture surface with no veins due to fast catastrophic shear at the end of the fracture stage, where there is no enough time veins formation.

It was observed that in some of the modified $Cu_{47}Ti_{33}Zr_{11}Ni_7Si_1Sn_1$ alloys that have been subjected to the same compression failure tests, two interpenetrating cones appear on the fracture surface. The top of each cone is characterized by severe melting due to the release of the load at the final event of fracture in this very limited area, as presented in Fig. 11. The last event of melting is limited to this spot, since the rest of the surface deforms by shear before reaching this abrupt fracture event. Figure 12 displays the fracture surface and the cone apex where severe melting took place and liquid-like droplets show up. The conical shape fracture surface was linked to the formation of the very fine nanocrystals in this sample, which enhance the homogeneity of the deformation, leading to the formation of multiple-shear planes instead of single shear plane normally encountered in bulk metallic glasses [36]. Such improvement in the homogeneity of the deformation shows up as larger total strain at fracture relative to the same composition without additions of Si and Sn (see Fig. 6a).

Close investigation of the conical surface of the fractured specimen shows that the two layers (veins and featureless area) deform at different rates, since the vein-like layer is extruded out of the surface relative to the featureless layer, as shown in Fig. 12. Figure 12b, c displays three-dimensional view of the veins, which are

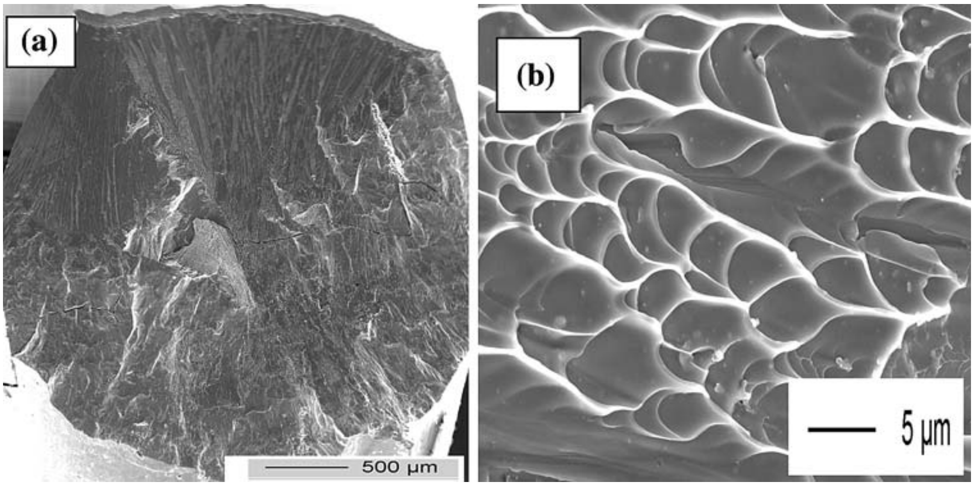

Fig. 8 For the unmodified Cu-based alloy **a** SEM of fractured and **b** Magnification of the veins morphology

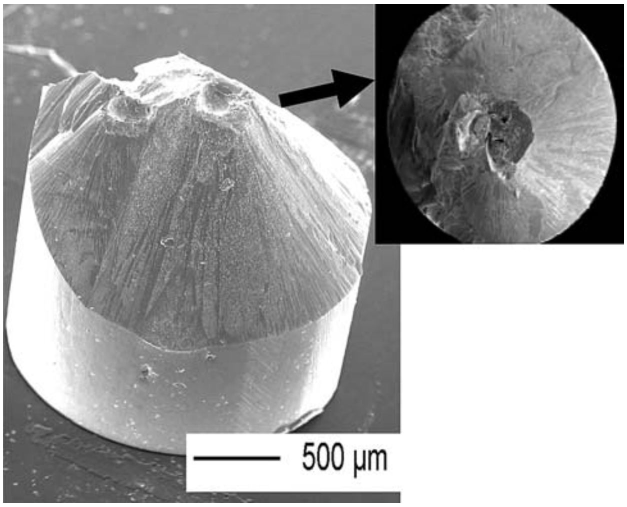

Fig. 9 Conical shape failure formation of the modified $Cu_{47}Ti_{33}Zr_{11}Ni_7Si_1Sn_1$ alloy

10 μm in height. This implies that the vein-like layer flows more readily and a normal stress to such layers exists and causes such flow. Zhang et al. [27] argued that such normal stresses are important for the fracture process of BMGs. Also, this difference in flow behavior of the two layers could imply that the less deformed layer exhibits a higher flow stress due to the presence of nanocrystallites or the formation of such crystallites during deformation.

A mechanism for the aggregation of small nanocrystallites during deformation to a region with a high density of nanocrystallites and another with lower density, leading to such differences, was proposed earlier [9]. Also, the formation of nanocrystals in shear bands and nanocrystallization during nano-indentation was previously reported [31–33]. The viscosity of the composite (BMG and nanoparticles) in the region where less nanocrystals exist will be lower leading to a lower critical shear stress and a more readily plastic deformation. TEM investigation of the

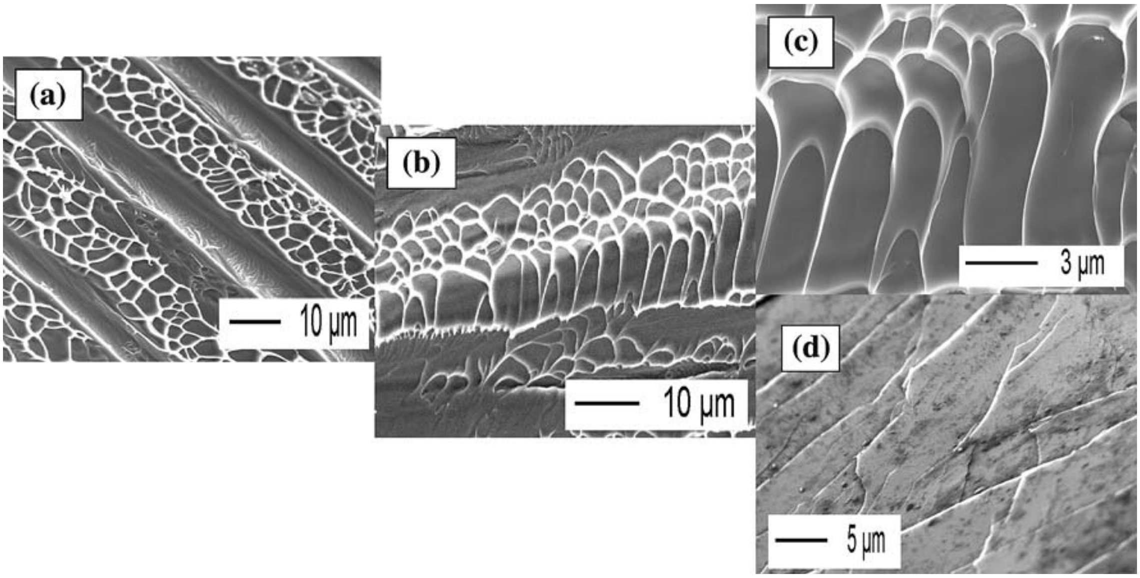

Fig. 10 Mixed fracture mode of the modified $Cu_{47}Ti_{33}Zr_{11}Ni_6Si_1Sn_2$ alloy, **a** overview, **b** Vein type, **c** mixed mode and **d** catastrophic zone

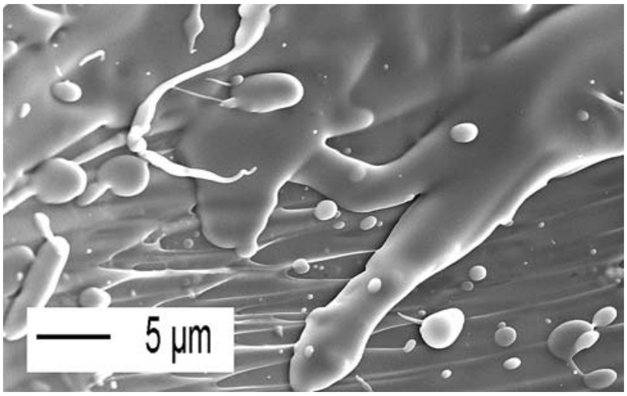

Fig. 11 Severe melting of the cone apex at the event of fracture the modified $Cu_{47}Ti_{33}Zr_{11}Ni_6Si_1Sn_2$ alloy

modified $Cu_{47}Ti_{33}Zr_{11}Ni_7Si_1Sn_1$ alloy, as presented in Fig. 12a–c. The conical fracture surface displays a structure of an amorphous matrix with very fine nanocrystallites of 2–5 nm size, which was also verified early through the bright-field image and the corresponding diffraction pattern (Figs. 3b and 4a). To make sure that the formation of conical surface was reproducible, several specimens of the modified $Cu_{47}Ti_{33}Zr_{11}Ni_7Si_1Sn_1$ alloys were tested and the phenomena were sustained.

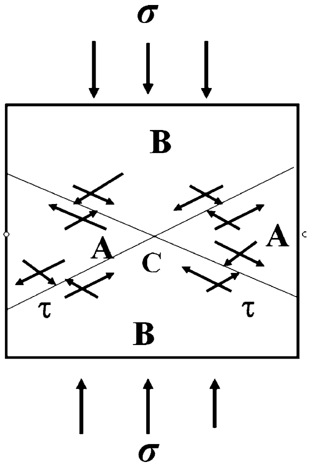

Fig. 13 A schematic forces representation of a proposed mechanism for the formation of the conical fracture surface under compression testing

There has been investigation on the interaction of shear bands with microstructure in BMG [32], the direct observation of crystallization within the shear bands of aluminum-based amorphous alloys induced by bending are reported. The crystals are face-centered cubic aluminum, and seem to form as a consequence of local atomic rearrangements in regions of high plastic strain, this mechanical deformation can explain the formation of the high strength amorphous–nanocrystalline composites [32]. A schematic representation of a proposed mechanism for the formation of the conical fracture surface under compression testing is presented in Fig. 13. Multi-shear planes with fracture angles deviating from 45°, intersect at point ‘C’. A difference in angle will lead to the development of two stress components parallel to the conical surface and a stress component normal to it, which in turn plays an important role in the fracture process [24–26]. The force balance shown in Fig. 13, indicates that the cone surface in part ‘B’ is subjected to a normal tensile stress in addition to the shear stress. This hypothesis is corroborated by the displacement in height of the different layers relative to each other. As the crack propagates on the fracture surface

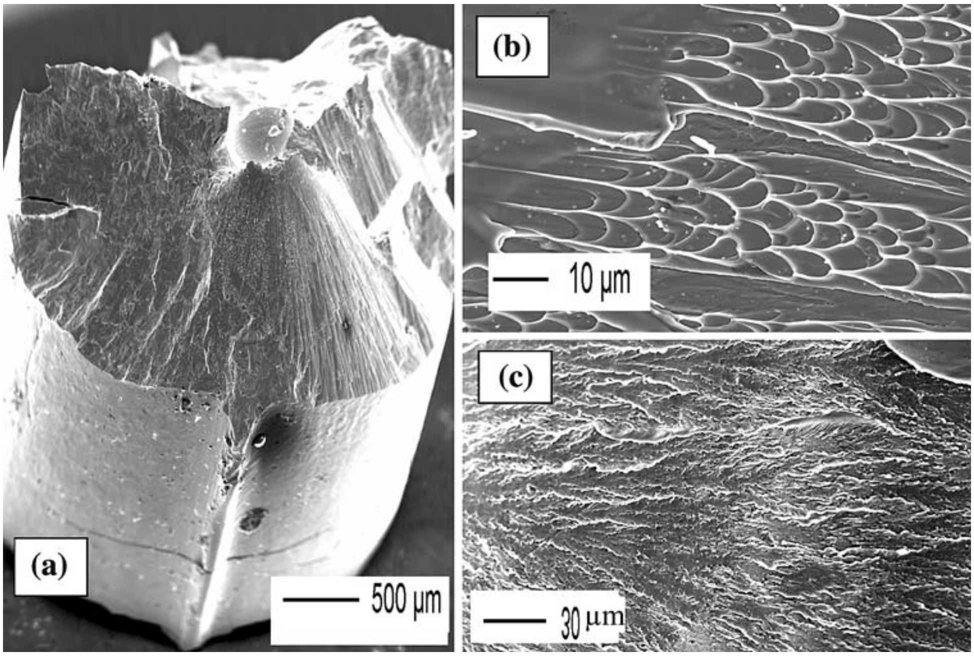

Fig. 12 For the modified $Cu_{47}Ti_{33}Zr_{11}Ni_7Si_1Sn_1$ alloy **a** Multilayered structure, **b** extruded veins layer and **c** magnified view of B

(between A and B), part A will be forced out leading to the formation of such a cone. The existence of such difference in height (~ 10 µm) between the two layers indicates that extensive plastic deformation takes place on the micrometer scale and also reflects the difference in flow properties between each layer.

As the Sn content increases to 2 at.% (as of the modified $Cu_{47}Ti_{33}Zr_{11}Ni_6Si_1Sn_2$ alloy), the fracture mode becomes mixed. Some parts of the fracture surface have cone-like features, as shown in Fig. 10. The conical surface exhibits vein-like features, while the area fracturing last shows a very smooth surface with almost no veins. The flow deformation and fracture behavior depends on the nature, size, volume fraction, and distribution of nanocrystals or quenched-in crystalline phase. The formation of a mixed fracture mode indicates that the conical morphology already appears for a critical volume fraction and size of nanocrystallites. The size of the nanocrystalline particles relative to the width of the shear bands is critical in inducing inhomogeneity in the flow deformation and micro-crack formation [37]. The nanoscale particles on the other hand, may increase the viscosity of the flow but do not form micro-cracks, leading to particle strengthening of the metallic glass.

Conclusions

Alloying of $Cu_{47}Ti_{33}Zr_{11}Ni_{9-(x+y)}$ ($x = $ Si, $y = $ Sn, $0 \leq x \leq 1$, $0 \leq y \leq 2$) BMGs changes the mode of fracture from single flat shear plane type, which is a characteristic feature of fracture for bulk metallic glasses to a multiple-shear plane mode, leading to the formation of a conical shaped fracture surface in uniaxial compression. In some cases, a mixed fracture mode was encountered. Si and Sn modification of the investigated Cu-base BMG promotes the formation of very fine (2–5 nm), homogeneously distributed crystallites. Such crystallites enhance the distribution of shear bands leading to a more uniform deformation.

At room temperature compression tests reveal fracture strength of 2000 MPa, elastic modulus of 127 GPa, and 1.8% fracture strain for the unmodified basic alloy. Whereas, the modified alloy exhibits a fracture strength of 2179 MPa, the elastic modulus reaches 123 GPa, and 2.4% fracture strain. So, with the addition of 1 at.% Si and Sn. The local enhancement of deformation homogeneity by precipitation of very fine nanocrystalline particles (due to composition modification) results in a multiple-plane fracture surface formation and an increase in the strain to fracture by about 25%, and the fracture strength improves by 9%. The fracture behavior under compression conditions exhibits a conical shape similar to that produced by tensile testing of ductile alloys. The appearance of the compressive fracture surface of such of nano-composites, such as viscous flow traces, vein pattern morphology, and localized melting, indicates a typical ductile fracture mode, and corresponds with well-known deformation behavior of amorphous alloys. This could be explained by the formation of homogeneously distributed nano-size (2–5 nm) precipitates, which changes the mode of fracture of the metallic glass from single to multiple shear plane mode leading to the conical shape fracture surface morphology.

References

1. Zhang T, Inoue A, Masumoto T (1991) Mater Trans JIM 32(11):1005
2. Inoue A (1998) Acta Mater 48(1):279
3. Gilbert CG, Ritchie RO, Johnson WL (1997) Appl Phys Lett 71:476
4. Conner D, Rosakis AJ, Johnson WL, Owen DM (1997) Scr Mater 37(9):1373
5. Zhang QS, Zhang HF, Deng YF, Ding BZ, Hu ZQ (2003) Scr Mater 49(4):273
6. El-Hadek MA, Kassem M (2008) Int J Mech Mater Des 4(3):279
7. Hays CC, Kim CP, Johnson WL (2000) Phys Rev Lett 84(13):2901
8. Glade SC, Löffler JF, Bossuyt S, Johnson W (2001) J Appl Phys 89:1573
9. Bae DH, Lim HK, Kim SH, Kim DH, Kim WT (2002) Acta Mater 50(7):1749
10. Schroers J (2007) Acta Mater 56(3):471
11. Park ES, Lim HK, Kim WT, Kim DH (2002) J Non-Cryst Solids 298(1):15
12. Choi-Yim H, Busch R, Johnson WL (1998) J Appl Phys 83(12):7993
13. Spaepen F, Taub A (1983) Amorphous metallic alloys. Butterworth, London
14. Nishiyama N, Inoue A (1997) Mater Trans JIM 38(5):464
15. Volkert CA, Lilleodden ET (2006) Phil Mag 86(33–35):5567
16. El-Hadek MA, Kaytbay S (2008) Strain. doi:10.1111/j.1475-1305.2008.00552.x
17. Bruck HA, Christman T, Rosakis AJ, Johnson W (1994) Scr Metall Mater 30(4):429
18. Scudino S, Surreddi KB, Sager S, Sakaliyska M, Kim JS, Löser W, Eckert J (2008) J Mater Sci 43(13):4518. doi:10.1007/s10853-008-2647-5
19. Bhowmick R, Majumdar B, Misra DK, Ramamurty U, Chattopadhyay K (2007) J Mater Sci 42(22):9359. doi:10.1007/s10853-007-1856-7
20. Donovan PE (1988) Mater Sci Eng 98:487
21. Lowhaphandu P, Montgomery SL, Lewandowski JJ (1999) Scr Mater 41(1):19
22. Wright WJ, Saha R, Nix WD (2001) Mater Trans JIM 42:642
23. Wright WJ, Hufnagel TC, Nix WD (2003) J Appl Phys 93(3):1432
24. Donovan PE (1989) Acta Mater 37:445
25. Chen D, Takeuchi A, Inoue A (2007) J Mater Sci 42(20):8662. doi:10.1007/s10853-007-1830-4
26. Zhang ZF, Eckert J, Schultz L (2003) Acta Mater 51(4):1167
27. Liu CT, Heatherly L, Easton DS, Carmichael CA, Schneibel JH, Chen CH (1998) Metall Mater Trans A 29(7):1811
28. Qiu K, Hao DZ, Ren YL, Zhang H (2007) J Mater Sci 42(9):3223. doi:10.1007/s10853-006-0238-x
29. Bian Z, He G, Chen GL (2002) Scr Mater 46(6):407
30. Kim HS, Bush MB, Esstrin Y (2000) Acta Mater 48(2):493

31. Palmqvist S (1963) Jernkontoreets Ann 147:107
32. Chen H, He Y, Shiflet GJ, Poon SJ (1994) Nature 367:541
33. He Y, Shiflet GJ, Poon SJ (1995) Acta Mater 43(1):83
34. Gao MC, Hackenberg RE, Shiflet GJ (2003) Appl Phys Lett 83(13):2575
35. Leamy HJ, Wang TT, Chen HS (1972) Metall Mater Trans B 3(3):699
36. Calin M, Eckert J, Schultz L (2003) Scr Mater 48(6):653
37. Bian Z, Chen GL, He G, Hui XD (2001) Mater Sci Eng A 316(1–2):135